Biophysical Journal
Article

Biophysical Society

Competition between deformation and free volume quantified by 3D image analysis of red blood cell

Mehrnaz Babaki,[1,2] Dmitry A. Fedosov,[3] Amirreza Gholivand,[1,2] Joeri Opdam,[4] Remco Tuinier,[4] and Minne Paul Lettinga[1,2,*]

[1]Institute of Biological Information Processing IBI-4, Forschungszentrum Jülich, Jülich, Germany; [2]Laboratory for Soft Matter and Biophysics, KU Leuven, Leuven, Belgium; [3]Institute of Biological Information Processing and Institute for Advanced Simulation, Forschungszentrum Jülich, Jülich, Germany; and [4]Laboratory of Physical Chemistry, Department of Chemical Engineering and Chemistry, and Institute for Complex Molecular Systems (ICMS), Eindhoven University of Technology, Eindhoven, the Netherlands

ABSTRACT Cells in living organisms are subjected to mechanical strains caused by external forces like overcrowding, resulting in strong deformations that affect cell function. We study the interplay between deformation and crowding of red blood cells (RBCs) in dispersions of nonabsorbing rod-like viruses. We identify a sequence of configurational transitions of RBC doublets, including configurations that can only be induced by long-ranged attraction: highly fluctuating T-shaped and face-to-face configurations at low, and doublets approaching a complete spherical configuration at high, rod concentrations. Complementary simulations are used to explore different energy contributions to deformation as well as the stability of RBC doublet configurations. Our advanced analysis of 3D reconstructed confocal images of RBC doublets quantifies the depletion interaction and the resulting deformation energy. Thus, we introduce a noninvasive, high-throughput platform that is generally applicable to investigate the mechanical response of biological cells to external forces and characterize their mechanical properties.

SIGNIFICANCE Deformability is vital for cell function, as cells experience external forces such as overcrowding and flow in living matter. We introduced a generic platform to investigate cell deformability, which consists of a noninvasive, high-throughput toolbox. It combines dispersed rod-like viruses to induce long-ranged depletion attraction to deform cells with advanced 3D confocal image analysis. We applied our approach to pairs of red blood cells and found a plethora of transitions in the shape of the resulting doublets with increasing rod concentration. These transitions are understood on the basis of our toolbox by quantification of the underlying competition between depletion and deformation energies. The presented platform is general and can elucidate the cell mechanics under physiological and pathological conditions.

INTRODUCTION

The attractive depletion force is a crowding phenomenon, which plays an important role in many biological processes (1,2). It is suggested that depletion accounts for phase separation between the nucleoid and the cytoplasm within cells (3,4). On a larger scale, depletion has been used to explain the mechanism behind the aggregation of red blood cells (RBCs) into a rouleau, a cylindrical stack of RBCs (5–7), which is a crucial element of blood circulation (8–11). The attractive force in depletion interaction results from small particles, depletants, that are excluded from a zone around larger particles, called the depletion layer. When the depletion layers of two large particles overlap, this results in an osmotic imbalance so that the large particles are pushed together. Though the exact force can ideally be calculated based on the ground-breaking theory of Asakura and Oosawa (12), depletion forces cannot readily be calculated for biological systems. One reason is that specific interactions between the small and big particles often cannot be neglected. Moreover, most biological systems have irregular and deformable shapes both on a macromolecular level (13,14) as well as the cellular level (15). The softness (16,17) and shape (18) of the depletant have been accounted for, as well as complex geometries of the particles, for example in the lock-and-key principle (19). However, much less is known about the effect of the deformation of particles. Depletion-induced particle deformation can lead to more compact configurations and thus a decrease in excluded volume for the depletants ΔV_{ex}, as the difference

Submitted November 25, 2022, and accepted for publication March 21, 2023.

*Correspondence: p.lettinga@fz-juelich.de

Editor: Timo Betz.

https://doi.org/10.1016/j.bpj.2023.03.030

between the depletion zone around a compact doublet and the depletion zone of two separate undeformed cells is not only achieved by optimizing the configuration as in the traditional theories (see Fig. 1 *B*) but also through deformation (see Fig. 1 *C*). However, this gain in free volume comes at the cost of elastic energy due to deformation.

In this article, we show how the interplay between depletion and bending can be quantified for two RBCs in a doublet by combining two tools: the use of rod-like viruses as a biomolecular crowding agent and extensive analysis of 3D confocal images. Numerical simulations (15,20–22) of vesicles and RBCs in a doublet already showed that the morphology of aggregates depends on the interplay between short-range adhesion energy, mimicking the depletion-induced attraction, and the bending rigidity of the membrane (21), the shear elasticity (15), and the surface tension (22). The simulations are in qualitative agreement with 2D image analysis of doublets induced by dextran (15, 23), which is a macromolecule known to stimulate rouleaux formation (20). However, in previous studies, the deformation of RBCs has not been imaged in 3D, which impedes the reliable quantification of the induced deformation. Moreover, macromolecules used as depletants can be present between the two cells in contact, as their size is similar to the thickness of the glycocalyx, which is a soft brush of biomolecules on the cell surface. These macromolecules can then directly bridge the two cells, in addition to the imposed depletion interactions (24).

The *fd* virus that we use is a monodisperse, very slender (length: 880 nm, diameter: 6.6 nm) and stiff (persistence length: 2.2 μm) colloidal rod. As *fd* does not bind to the cells (25), bridge formation is excluded, and they yield a pure depletion interaction over considerably longer distances than traditionally used polymeric depletants. This has the advantage that their size exceeds the thickness of the glycocalyx, and strong deformations can be induced at relatively low volume fractions. Given the natural monodispersity of the viruses, *fd* is amenable to theoretical analysis, as was shown for the phase behavior of rod-sphere mixtures (26, 27), in contrast to chromonic systems (28). In order to calculate the depletion energy, we employ our second tool, namely extensive image analysis of 3D confocal microscopy images of RBC doublets. We use this tool to calculate ΔV_{ex} and also to measure the resulting deformation in terms of the change in the membrane curvature of the cells, yielding the increase in bending energy. We complement the experiments with simulations, where the attraction potential is implemented either as the excluded volume interaction of the explicit rods (i.e., a direct depletion interaction) or as a pairwise adhesion between two cells modeled by a Lennard-Jones (LJ) potential.

In general, exerting mechanical forces on cells results in cell deformation (29,30). Understanding cell deformation under external load is key to a full comprehension of the behavior of cells under mechanical loadings, such as cellular growth, where the mechanical stresses can affect tissue proliferation (31); cellular apoptosis initiated by mechanical stimuli (32); and overcrowding in tissue leading to live-cell extrusion or delamination (33,34). Cell deformation is most prominent in blood flow, ranging from endothelial cells deformation (35) and deformation of leukocytes adhering to the endothelial cells (36) to the extreme deformation of RBCs themselves as they pass through narrow microcapillaries with a diameter smaller than the diameter of RBCs (37). Established techniques to investigate cell response to applied forces and to quantify the deformability of biological cells (38,39) are micropipette aspiration (40–43), optical trapping (44,45), and atomic force microscopy (46–48), applying forces ranging from tens to

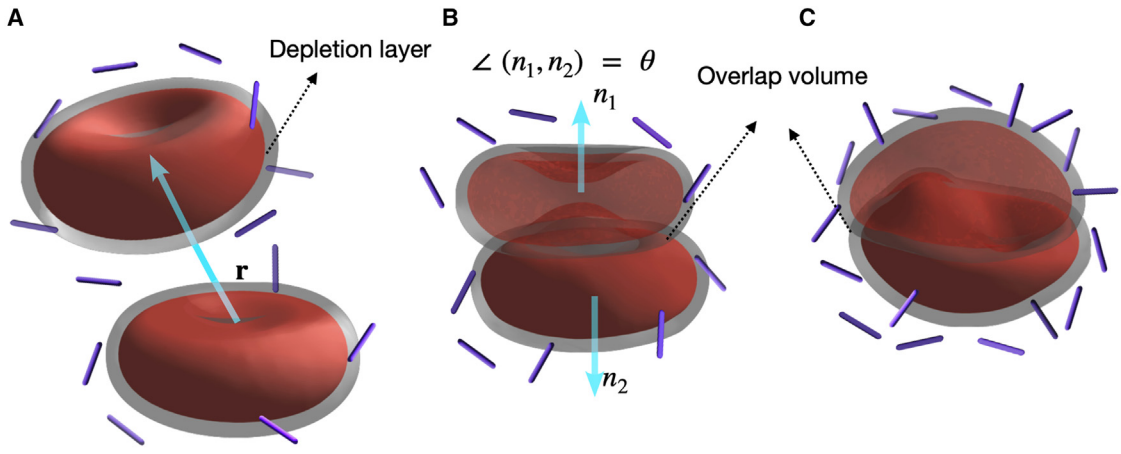

FIGURE 1 Schematic representation of two RBCs in a suspension of nonadsorbing rods. (*A*) The two cells are far apart. (*B*) At low rod concentration, c_{rod}, RBCs preserve their biconcave shape and do not deform. Also, there is a gap between the cells. The overlap volume, V_{ov}, is where the depletion layer of the two RBCs overlaps. (*C*) At high c_{rod}, the cells are in full contact and have a deformed shape to decrease the volume excluded to the rods by the doublet. The gray layer around the cells represents the depletion layer.

hundreds of pN. Despite their success, these techniques are experimentally involved and limited to single-cell measurements, while they can affect the mechanical properties of the cells. By combining the tool of long-ranged attraction as induced by colloidal rods and 3D image analysis, we introduce a noninvasive method with high throughput to obtain mechanical features of cells by quantifying the balance between hydro-static pressure when two cells are squeezed together and the resulting deformation.

We first introduce the energies that determine the shape of the doublet, namely the depletion and elastic energies. We then present a cascade of observed configurations, their relative contributions as a function of the depletion force, and the underlying dependence of excluded volume and bending energy, aided by the simulations. Thus, we show how the cascade of configurational transitions occurs as a competition between long-ranged attraction mediated by rod-like depletants and the deformability of RBCs.

MATERIALS AND METHODS

Discretized model for elastic energy contributions

The changes in the elastic energy (E_{elas}) of RBC membrane due to deformation consist of four contributions,

$$E_{elas} = E_{shear} + E_{bend} + E_{area} + E_{vol}, \quad (1)$$

where E_{shear} represents an in-plane elastic energy and E_{bend} corresponds to the bending resistance of the membrane. E_{area} and E_{vol} represent the surface area and volume constraints, which are used to maintain a nearly constant RBC area and volume. In both experiments and simulations, the surface of the RBC is discretized into a triangulated network with N_v vertices, N_e edges, and N_f triangular faces (49,50). To compute changes in the elastic energy (ΔE_{elas}), the first three contributions are considered in simulations because E_{vol} remains nearly constant. In the experiment, it is only possible to calculate E_{bend}, as triangulation of the RBC surfaces is done after the deformation. For a triangulated RBC surface, E_{shear} is given by (49,50)

$$E_{shear} = \sum_{i=1}^{N_e} \frac{k_B T \ell_m \left(3x_i^2 - 2x_i^3\right)}{4p(1-x_i)} + \sum_{i=1}^{N_e} \frac{k_p}{\ell_i}, \quad (2)$$

where the first term is an attractive worm-like chain potential and the second term is a repulsive potential with a strength coefficient k_p. In the attractive potential, k_B is the Boltzmann constant, T is the temperature, p is the persistence length, ℓ_i is the extension of edge i, ℓ_m is the maximum edge extension, and $x_i = \ell_i/\ell_m$. The bending resistance of the membrane is discretized as (51)

$$E_{bend} = \frac{\kappa}{2} \sum_{i=1}^{N_v} \frac{1}{\sigma_i} \left[\boldsymbol{n}_i \cdot \left(\sum_{j(i)} \frac{\sigma_{ij}}{r_{ij}} \boldsymbol{r}_{ij} \right) \right]^2, \quad (3)$$

where κ is the bending rigidity, $\boldsymbol{n}_i$ is a unit normal of the membrane at vertex i, and $\sigma_i = (\sum_{j(i)} \sigma_{ij} r_{ij})/4$ is the area of dual cell of vertex i. $j(i)$ stands for all neighboring vertices linked to the vertex i, and $\sigma_{ij} = r_{ij}[\cot(\theta_1) + \cot(\theta_2)]/2$ is the length of the bond in dual lattice, with angles θ_1 and θ_2 being the two angles opposite to the shared bond vector $\boldsymbol{r}_{ij}$. Finally, the area dilation energy is given by (49,50)

$$E_{area} = \frac{k_a (A - A_0)^2}{2A_0} + \sum_{i=1}^{N_f} \frac{k_d \left(A_i - A_i^0\right)^2}{2A_i^0}, \quad (4)$$

where k_d and k_a are local area and total surface area constraint coefficients, respectively. A_i is the instantaneous local area of each triangle in simulations and A_i^0 is its desired or targeted value. A is the instantaneous area of the whole RBC, and A_0 is the targeted area of the RBC. The first term in Eq. 4 on the right-hand side controls the total membrane area, while the second term represented by the sum over triangular elements controls local area dilation of the membrane.

Depletion energy calculation

When the distance between the center of mass of the rod and the surface of, for example, an RBC is smaller than half the rod length, then the number of configurations for the rod becomes limited. Hence, there is an effective layer around surfaces depleted from rods, called the depletion layer. Thus, the total volume excluded for the rods (V_{ex}) is equal to the volume of the objects plus the depletion layer around these objects. When the depletion layers of two rigid objects are separated by a distance $\boldsymbol{r}$ overlap, then the excluded volume is reduced by the overlap volume $V_{ov}(\boldsymbol{r})$ between the objects, resulting in an attractive depletion interaction between them. The effective attractive interaction potential between objects due to the presence of colloidal rods can be written as (52)

$$\Delta E_{dep}(\boldsymbol{r}) = -\Pi V_{ov}(\boldsymbol{r}), \quad (5)$$

where ΔE_{dep} is the change in the depletion potential and Π is the osmotic pressure difference of depletants between the bulk (i.e., far from the RBCs) and that in the depletion layer.

In the case of RBCs, not only is the distance $\boldsymbol{r}$ between cells important but so are their relative position and orientation given by θ (see Fig. 1, *A* and *B*). Furthermore, the RBCs can deform in response to depletion forces.

$V_{ov}^{conf} = V_{ex}(\boldsymbol{r} \to \infty) - V_{ex}(\boldsymbol{r}, \theta)$ defines the gain in the accessible volume for the rods due to the configuration of two undeformed RBCs at low concentrations, where $\Delta E_{elas} = 0$. In this case, the change in the depletion energy E_{dep}^{conf} can be written as

$$\Delta E_{dep}^{conf} = -\Pi V_{ov}^{conf}. \quad (6)$$

With increasing rod concentration, the configuration of the two undeformed RBCs will proceed toward a maximal overlap between them. After the most compact configuration of two cells with $V_{ex}(\boldsymbol{r}^{min}, \theta^{min})$ is reached for some $\boldsymbol{r}^{min}$ and θ^{min}, V_{ex} can decrease further with increasing c_{fd} only through RBC deformation. Hence, we also need to consider the gain in free accessible volume for depletants due to RBC deformation, $V_{ov}^{def} = V_{ex}(\boldsymbol{r}^{min}, \theta^{min})|_{\Delta E_{elas}=0} - V_{ex}(\boldsymbol{r}^{min}, \theta^{min}, \Delta E_{elas}))$. In this case, the difference in excluded volume between deformed and undeformed RBCs in a doublet should be considered. As a result, there is an extra contribution to the change in the depletion energy, given by

$$\Delta E_{dep}^{def} = -\Pi V_{ov}^{def}. \quad (7)$$

To estimate the osmotic pressure, we use an expression from the scaled particle theory for colloidal rods modeled as hard spherocylinders (53):

$$\frac{\Pi V_r}{k_B T} = \frac{\varphi_r}{1-\varphi_r} + \frac{3\gamma(\gamma+1)}{3\gamma-1} \left(\frac{\varphi_r}{1-\varphi_r}\right)^2 + \frac{12\gamma^3}{(3\gamma-1)^2} \left(\frac{\varphi_r}{1-\varphi_r}\right)^3. \quad (8)$$

Here, V_r is the volume of a rod, and φ_r is the volume fraction of rods. γ is related to the aspect ratio of the rods, L/D, as $\gamma = 1 + \frac{L}{D}$, with L and D being the length and diameter of the rods, respectively. In the case of *fd* virus, L is 880 nm, and D is 6.6 nm. The effective diameter of the *fd* is larger than 6.6 nm due to the electrostatic repulsion between rods. At the solution ionic strength of 150 mM, the D_{eff} of the rods is 10 nm (54). We have to consider, however, that the rods themselves have a significant excluded volume. Our recent study shows that for a volume fraction of rods above approximately 0.0023, there is a nearly linear deviation between theory and experiment, suggesting that φ_r in Eq. 8 should be replaced by (27)

$$\varphi_r \rightarrow \varphi_r - (\varphi_r - 0.0023) \times 0.55 \quad \text{for } \varphi_r > 0.0023. \tag{9}$$

We have direct access to $V_{ex}(\boldsymbol{r}, \theta)$ through the 3D reconstruction of RBC shapes using triangulated meshes and normal vectors at the surface of cells (see image analysis section and Fig. 2 *A*). $V_{ex}(\boldsymbol{r}, \theta)$ is calculated by adding a depletion layer around the cells with a thickness equal to a quarter of the length of the rods (for more details, see the supporting material). In the second step, the volume where the depletion layers of the two cells overlap is removed. Third, a new triangular mesh is created at the surface of a doublet with the adjusted depletion layer, which determines the excluded volume of the doublet. Using Eqs. 8 and 5 and the obtained excluded volume, the depletion energy for each configuration is then computed.

Sample preparation

All experiments are performed using fresh blood taken by finger pricking from healthy donors. The blood is collected into tubes where the walls are coated with anticoagulants such as EDTA. After washing the RBCs three times (500× *g*, 10 min) in phosphate-buffered solution, RBCs are labeled with CellMask Green Plasma Membrane Stain from Thermo Fisher Scientific (Waltham, MA, USA).

Rods are used to induce depletion interactions, as they are very effective depletants (55), which has been shown experimentally through a direct measurement of the depletion potential (56,57). We use a wild-type of rod-like *fd* virus that is grown and purified following standard biochemical protocols (58). *fd* virus has a diameter of 6.6 nm and a length of 880 nm. The samples are prepared by redispersing labeled RBCs at the hematocrit of 1% in a density-matched medium (a mixture of phosphate-buffered solution and OptiPrep [pH 7.4]) and adding *fd* from stock solutions to obtain different concentrations.

In the samples, beside RBC doublets, aggregates of more than two cells can also form. The frequency of their formation depends on the probability of cells to encounter each other, which is affected by the volume fraction of RBCs in the sample (kept constant at 1% in this study) and the diffusion rate of RBCs within the rod suspension.

Microscopy

The sample is then filled into the μ-slide channel from ibidi. The channels are sterilized and tissue culture treated, which makes the surface hydrophilic. Images are obtained at room temperature with an inverted microscope (Axiovert 200M, Zeiss, Jena, Germany). The left viewport of the microscope is coupled with a confocal unit (VT-Infinity3, VisiTech International, Sunderland, UK) and a high sensitivity camera (Andor iXon Ultra 888 EMCCD, Oxford Instruments, Abingdon, UK). Microscopy is performed using a 100× oil immersion objective and 0.5 μm steps in obtaining z stacks.

Image analysis

We used ilastik 1.3.3, an interactive machine-learning open-source software for (bio)image analysis to perform 3D reconstruction of the raw confocal data (59) and exported the resulting surfaces of RBCs as meshes. Then, MeshLab, an open-source mesh processing tool (60), was employed to

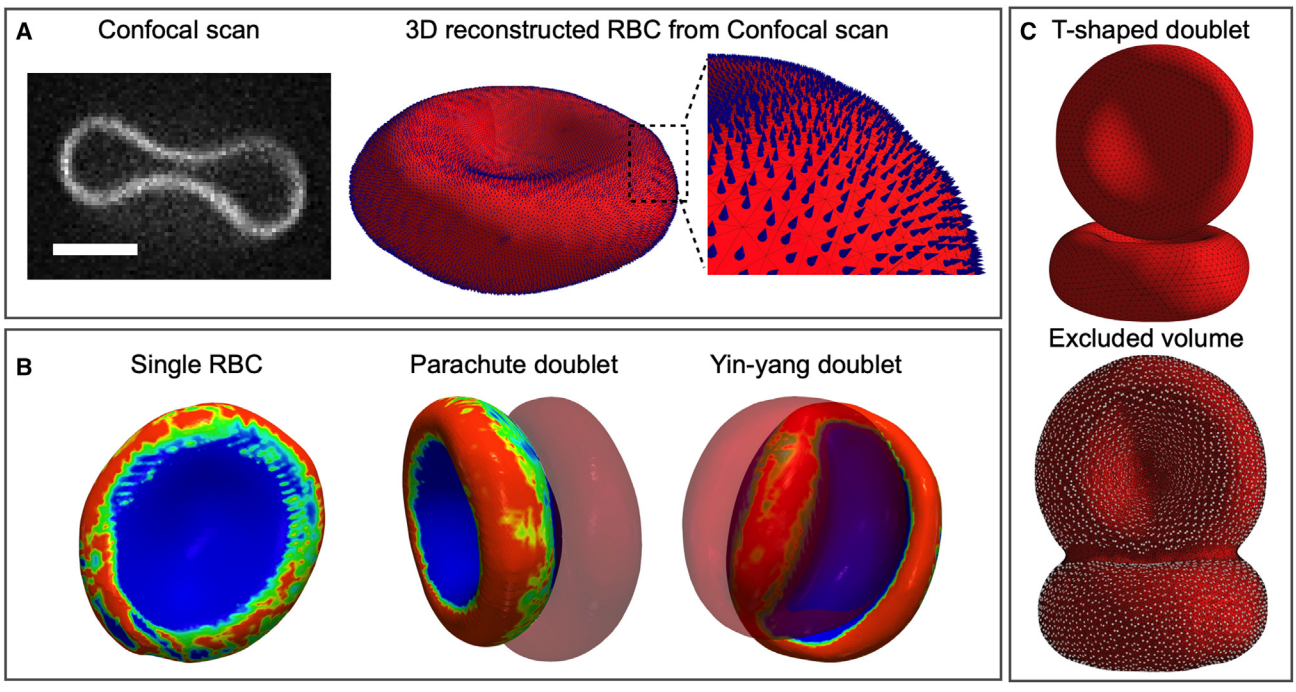

FIGURE 2 (*A*) A confocal scan of a single RBC and the corresponding 3D reconstructed cell with surface triangulation and corresponding normal vectors at each vertex. The scale bar is 3 μm. (*B*) 3D reconstruction of single RBCs and doublets with, from left to right, a biconcave shape, a parachute configuration, and a Yin-yang shape. The color coding indicates the local mean curvature of the cells, where red corresponds to the largest values and blue to the lowest values. (*C*) A 3D reconstructed RBC doublet (*top*) in a T-shaped configuration and the excluded volume of the same doublet for the depletants (*bottom*).

revise the meshes. The RBCs in experiments are fine meshed so that, on average, each RBC is meshed with $N_v \sim 14,000$ vertices with corresponding normal vectors (see Fig. 2 *A*). Plotly Python graphing library or MeshLab was used for the visualization of the 3D reconstructed RBCs. Discretized bending energy and excluded volume of the doublets were computed using an in-house Python-based code. In particular, the discretization of bending energy in Eq. 3 (51) was employed. The biconcave shape of a single RBC in equilibrium yields a bending energy of $E_b = 4307 \pm 221 k_B T$.

Simulation models

RBCs were modeled as triangulated surfaces with the total energy given in Eq. 1 (49,50). Each RBC consists of $N_v = 3000$ vertices, $N_e = 8994$ edges, and $N_f = 5996$ triangular faces. In addition to the shear deformation, bending, and area-dilation energies defined in Eqs. 2, 3, and 4, the volume conservation constraint is given by

$$E_{vol} = \frac{k_v (V - V_0)^2}{2V_0}, \tag{10}$$

where k_v is the volume-constraint coefficient and V_0 is the desired total volume of an RBC. For simulations with an adhesion potential, excluded-volume interaction as well as the attraction between two RBCs were modeled by the 12-6 LJ potential given by

$$E_{LJ}(r) = \epsilon \left[\left(\frac{r_{rep}}{r} \right)^{12} - 2 \left(\frac{r_{rep}}{r} \right)^{6} \right] \quad \text{for} \quad r < r_c, \tag{11}$$

where r is the distance between a pair of two vertices located at different RBCs, ϵ is the strength of the LJ potential, r_{rep} is a characteristic length of repulsion, and r_c is the cutoff distance. The attraction strength between two RBCs was modulated by changing ϵ.

For the case of explicit depletion interaction, the two RBCs were surrounded by a number of semiflexible polymers. The attractive LJ interaction between the RBCs from Eq. 11 was turned off by setting $r_c = \sqrt[6]{2} r_{rep}$ so that only excluded-volume repulsive interactions are present. Repulsion between polymers and RBCs is also mediated by the repulsive part of the LJ potential. Each polymer was modeled as a bead-spring chain of $N_p = 10$ particles. In the semiflexible polymer model, a harmonic spring potential and a harmonic angle potential between every pair of neighboring springs were employed. The strengths of these potentials were selected to be large enough so that the model approximates well nonextensible rigid rods. Dynamics of RBCs and semiflexible polymers was modeled by the Langevin equation

$$m \ddot{\mathbf{r}}_i = -\nabla_i E_{tot} - \gamma \dot{\mathbf{r}}_i + \sqrt{2\gamma k_B T} \xi_i(t), \tag{12}$$

where m is the particle mass, ∇_i is the spatial derivative at the position of particle i, and E_{tot} is the sum of all interaction potentials. The friction coefficient γ mimics embedding of the suspended components into a viscous fluid through the free-draining approximation. $\xi_i(t)$ is a Gaussian random process with $\langle \xi_i(t) \rangle = 0$ and $\langle \xi_i(t) \xi_j(t') \rangle = \mathbf{1} \delta_{ij} \delta(t - t')$ that represents thermal fluctuations. The positions and velocities of all particles were integrated using the velocity-Verlet algorithm (61). In simulations, cell properties correspond to average characteristics of a healthy RBC with a membrane area $A_0 = 133\ \mu m^2$, cell volume $V_0 = 93\ \mu m^3$, shear modulus $\mu = 4.6\ \mu N/m$, and bending rigidity $\kappa = 70 k_B T = 3 \times 10^{-19}$ J. The effective RBC diameter is defined as $D_r = \sqrt{A_0/\pi} = 6.5\ \mu m$ ($D_r = 6.5$ in model units), and the RBC reduced volume is equal to $V^* = 6V_0/(\pi D_r^3) \approx 0.64$. Note that the stress-free shape of an RBC elastic network (Eq. 2) is assumed to be an oblate spheroid with a reduced volume of 0.96. The biconcave shape of an RBC of $V^* = 0.64$ is obtained by deflating the stress-free spheroid with a reduced volume of 0.96. The length of each polymer is $L_p = 1.05\ \mu m$, and the thickness is $D_p = 0.15\ \mu m$. The persistence length of rods is equal to approximately $480\ L_p$. Note that the rod thickness D_p imposed through the characteristic length r_{rep} of the LJ potential defines a minimum resolution length in simulations. It is considerably larger than the thickness of *fd* virus used in experiments because a much finer resolution in simulations would tremendously increase their computational cost. All simulations were run on the supercomputer JURECA (62) at Forschungszentrum Jülich.

RESULTS

RBC doublet configurations

We observe a plethora of different configurations of doublets (see Fig. 3 *A*) when the *fd* concentration, c_{fd}, and thus the interaction strength, is increased from $c_{fd} = 0.125$ mg/ml to $c_{fd} = 12$ mg/ml. The onset of aggregation, where at least one RBC doublet can be observed within the observation time, is at approximately $c_{fd} = 0.05$ mg/ml. Relative contributions of the different configurations of RBC doublets as a function of the concentration of *fd* virus are shown in Fig. 3 *B*.

At the lowest concentration of $c_{fd} = 0.125$ mg/ml, the RBCs do not deform, and the doublets display a fluctuating gap between the two cells. At this concentration, a substantial number of doublets also exhibit a T-shaped configuration, where one RBC is located with its edge at the dimple of the other RBC. Furthermore, a few doublets show shifted gaps (see Fig. 3 *A*) between the two cells.

At $c_{fd} = 0.25$ mg/ml, shifted doublets are mainly observed and can be thought of as the most compact configuration of undeformed RBCs, for which $\theta_{min} \approx \pi$ and the in-plane component of $\mathbf{r}_{min}$ is about one RBC radius. At this concentration, the first doublets with a full contact, i.e., without the gap in a parachute configuration (see Fig. 3 *A*), are also detected. In the parachute configuration, one RBC has a concave-convex surface, while the other cell has either a concave-convex or concave-flat surface. The cell with a concave-flat surface experiences less deformation compared with the RBC with a concave-convex surface.

At $c_{fd} = 0.50$ mg/ml, another configuration called Yin-yang is observed. In this configuration, RBC doublets have a sigmoidal contact surface. It resembles the shifted gap configuration, but a significant membrane deformation is required to assure full contact. In the previous studies, this configuration has also been labeled as S-shaped (23). The fraction of full-contact configurations increases with increasing concentration until approximately $c_{fd} = 2.0$ mg/ml, where all doublets are in full contact either in parachute or Yin-yang configuration. Beyond $c_{fd} = 7.0$ mg/ml, most of the doublets take Yin-yang shape, and very few doublets have parachute shape. Larger values of *fd* concentration lead finally to a nearly spherical configuration of two cells since a sphere represents the most efficient packing of two RBCs in terms of excluded volume.

Compared with previous investigations (15,23), we have identified three new doublet configurations, including the T-shaped, doublets with a gap, and spherical doublets with

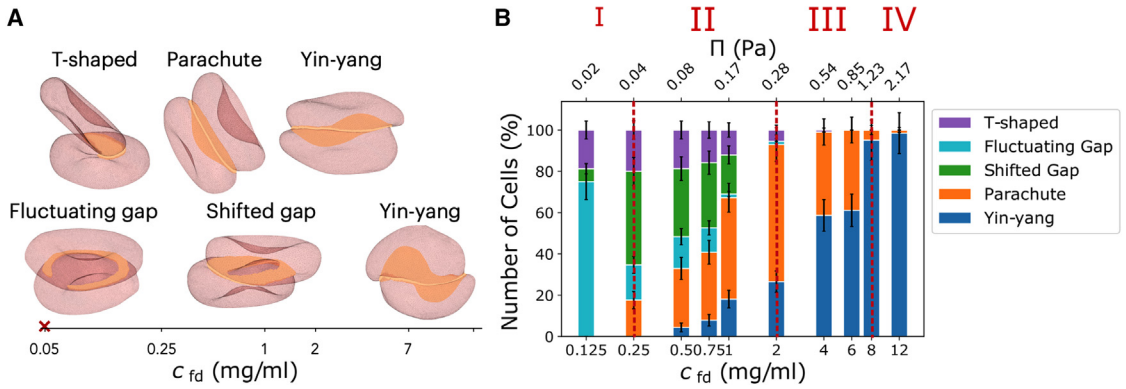

FIGURE 3 (*A*) Different configurations of RBC doublets reconstructed from confocal scans. The bright patches indicate contact between the cells. The red cross at the bottom left represents the onset of RBC aggregation in the presence of *fd* (25). c_{fd} represents the concentration of *fd*. (*B*) The corresponding distribution of these configurations, which were observed in experiments. Error bars are defined as the square root of the counts. We identify three transition regions, marked by *fd* concentrations of 0.25, 2, and 8 mg/ml *fd* and indicated with roman numbers. These regions represent different pathways for the minimization of the excluded volume, as discussed in the discussion section. See supporting material for confocal scans (Videos S1–S5) and Video S6 for the 3D reconstructed doublet in parachute configuration.

strong deformation of RBCs. Despite the fact that the spherical configuration has been suggested earlier (63), it has not yet been realized experimentally. In the following, the appearance of these configurations will be investigated in detail. To this end, parametrization of confocal images is employed to compute the excluded volume of a doublet as well as the local curvature of the cells and the corresponding bending energy. Furthermore, numerical simulations of two RBCs interacting via a depletion potential induced by explicitly modeled rods as well as via an attractive adhesion potential are used to corroborate experimental observations.

Changes in excluded volume

Compared with some depletants such as dextran, *fd* virus does not introduce any direct bridges between two RBCs and only mediates depletion interactions (25). Therefore, the gain in free energy for different doublet configurations can be calculated from the total excluded volume of a doublet for depletants, V_{ex}, using the rendered 3D reconstruction and triangulation of RBC shapes (see Fig. 2, *A* and *C*). V_{ex} as a function of the osmotic pressure Π/k_BT is plotted in Fig. 4 *A*, where Eqs. 8 and 9 are used to convert the concentration of rods into the osmotic pressure. Some values of V_{ex} at low *fd* concentration in Fig. 4 *A* are larger than the magnitude of the excluded volume for two single cells. The error bars are quite large because all cells are different. Furthermore, for the case of doublets with a gap, the excluded volume can be larger than that for two single cells due to the extra volume of the gap between the two cells. We can estimate the range of force applied by *fd* virus by converting the pressure to the force and measuring the contact surface between RBCs in a doublet (see supporting material for details). This yields a wide range of forces between 0.6 to 127 pN. Also, a large variance in the depletion energy in Fig. 4 *C* up to the osmotic pressure of about 1 Pa is due to large fluctuations in the overlap volume at low osmotic pressures. For example, at 4 mg/ml *fd*, we have observed Yin-yang doublets having different shapes (see Videos S4 and S5), even though for both of them, the contact surface has a sigmoid shape. In addition, differences in elastic properties of RBCs will contribute to the variations in doublet configurations at low attraction strengths. At large attraction strengths, these variations are significantly reduced. Nevertheless, the excluded volume decreases with increasing osmotic pressure. Excluded volumes calculated from experimental observations for different doublet configurations at a fixed c_{fd} often show overlapping ranges indicated by the error bars in Fig. 4 *A*. Thus, we cannot state with certainty whether some configurations such as the T-shape are thermodynamically more stable than others.

To assess the stability of the T-shaped and fluctuation/shifted gap configurations, numerical simulations of a doublet under a depletion potential mediated by explicitly modeled rods are performed (see the snapshots in Fig. 5, and Video S7 in supporting material). The rods in the simulation are 1.05 μm long and have a thickness of 150 nm. The simulations are performed at number densities of $n_b = 2.25$ and 3 μm^{-3} (see simulation models section for more details). To reduce the total computational cost, simulations were set such that a starting doublet configuration corresponds to either the T-shaped or face-to-face configuration. Face-to-face doublets are stable during the whole simulation for both number densities. However, the T-shaped doublet remains stable only for the large n_b, while at the low number density, the T-shaped configuration transits to a face-to-face doublet at long times.

The stability of the doublet configurations can be characterized by the distribution of angles between the normal vectors of the two cells (here, the eigenvector of the inertia tensor corresponding to the smallest eigenvalue), as

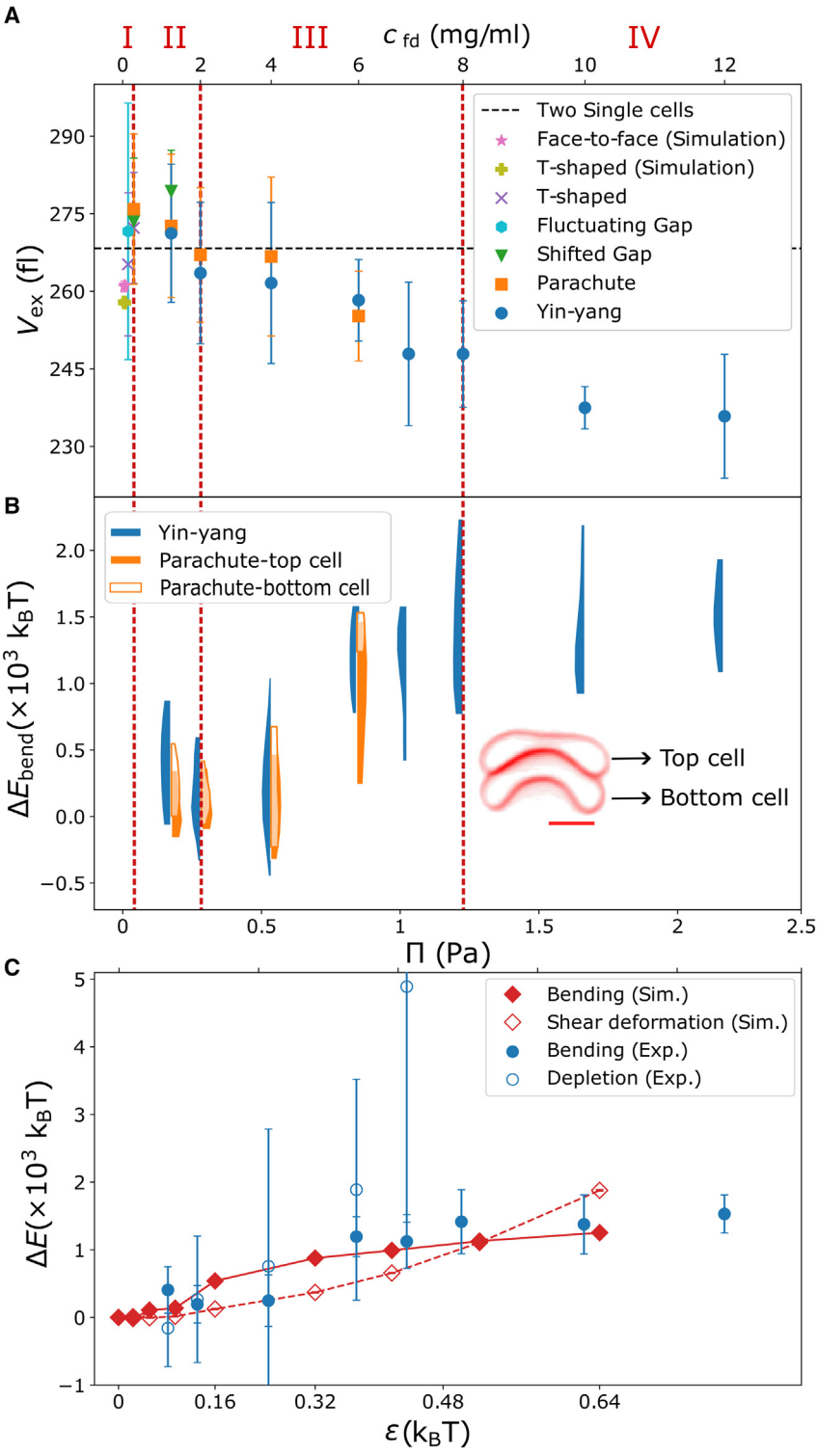

FIGURE 4 (*A*) Excluded volume for the depletants from different RBC-doublet configurations as a function of *fd* concentration. The dashed black line is the excluded volume of the two undeformed single cells. Error bars are given by the standard deviation of the data set, including doublets for calculating the excluded volume. (*B*) Change in the bending energy of single RBCs in Yin-yang and parachute doublets as a function of osmotic pressure or *fd* concentration. ΔE_{bend} is represented as a distribution of bending energies, where each sample of ΔE_{bend} corresponds to the bending energy computed over the whole triangulated surface of a single cell. For the parachute configuration, the bending energies of top and bottom cells are calculated separately, as the top cell experiences more deformation than the bottom cell (see the *inset*). The bending energy of Yin-yang doublets reaches a plateau beyond $\Pi \approx 1$ Pa. (*C*) Absolute changes in the experimental bending and depletion energies (*full and open blue circles*, respectively) and the bending and shear deformation energies (*full and open red diamonds*, respectively) from numerical simulations of the Yin-yang configuration as a function of osmotic pressure. Error bars in the experimental bending energy are given by the standard devation of the data set. Error bars for the depletion energy originate from the erros bars in the excluded volume values, see Eq. 5. The experimental bending and depletion energies are comparable up to $\Pi \approx 1$ Pa, after which the depletion energies become dominant. The simulated shear deformation energy becomes dominant over bending energy when the osmotic pressure increases beyond $\Pi \approx 1.3$ Pa. This suggests that the excess depletion energy is partially balanced by shear deformation energy.

doublets explore the state space in the simulation. The amount of experimental data is too limited for the construction of angle distributions, as observed doublets quickly bleach. Fig. 5 shows angle-dependent interaction potentials that are derived from the angle distributions, using the Boltzmann factor for both doublet configurations. The face-to-face configuration has a much steeper potential than the T-shape configuration, supporting a better stability of the face-to-face configuration. Nevertheless, the angle potential for the T-shaped doublet at the large number density is also relatively steep, so the T-shaped configuration is expected to remain stable. Note that the initial formation of

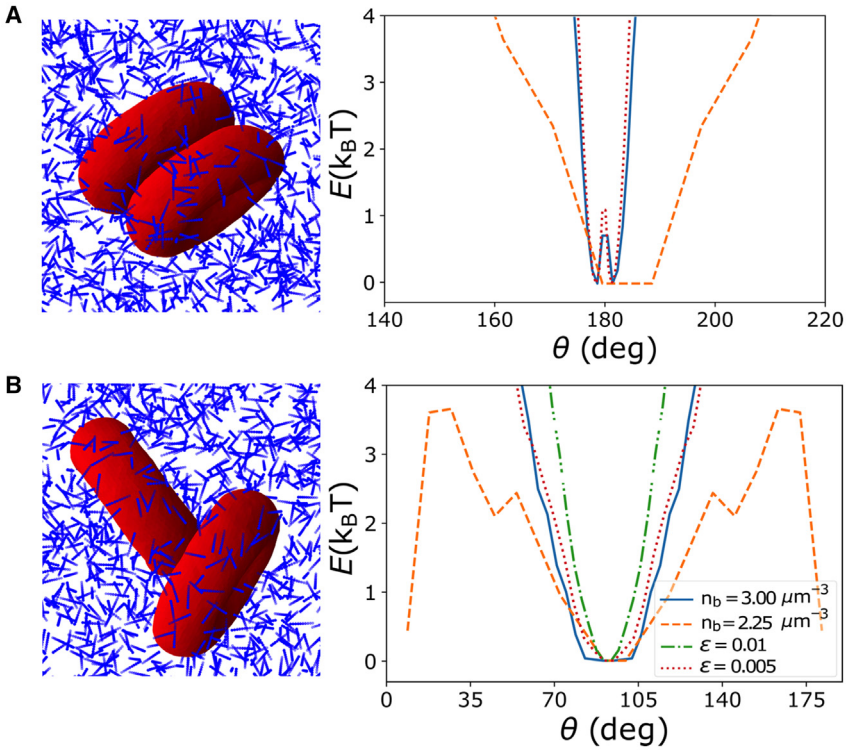

FIGURE 5 A snapshot of a doublet in simulations with explicit rods and the corresponding interaction potential for (*A*) face-to-face doublets and (*B*) T-shaped doublets. The interaction potentials originate from depletion potential induced by explicitly modeled rods as well as via an attractive adhesion potential and are calculated from distributions of angles of the relative orientation between two RBCs. Interaction potentials from simulations with an explicit attractive potential are also shown for two ε values. The legend is the same for both subfigures (*A*) and (*B*).

a T-shape is set by the probability that two RBCs approach each other at an angle close to 90°.

Fig. 5 also presents angle potentials obtained from simulations of a doublet formed by an attractive potential between vertices of two RBCs (i.e., without rods), as performed in a previous study (15). Interestingly, angle potentials from simulations with the attractive interaction compare well with those having depletion interactions mediated by explicit rods when the attraction strength ε is properly adjusted. As a first approximation, the strength ε of the LJ potential is guided well by the deformation of a doublet. It is also possible to relate ε to the strength of adhesion per unit area, as was done in (15). Note that this relation depends on the mesh size in RBC discretization and the range of the LJ potential. The comparison of angle potentials in Fig. 5 allows us to establish a mapping between different simulation models. For instance, the simulation with $n_b = 3\ \mu m^{-3}$ and the osmotic pressure of $\Pi = 8 \times 10^{-3}$Pa corresponds to the simulation with an attractive potential strength of $\varepsilon = 0.01$. Note that the depletion potential in Fig. 5 *A* for the low density of rods is not symmetric around 180° because there are strong fluctuations in the configuration of the doublet for weak depletion interactions. This requires very long simulations in order to statistically sample all possible states. The potential should be symmetric, and the asymmetry is likely due to the finite amount of statistics from performed simulations. The depletion potential in Fig. 5 *B* for $n_b = 2.25\ \mu m^{-3}$ shows a drop in the energy at $\theta = 0$ and 180 because the T-shaped doublet is not stable at this rod concentration. This drop in energy corresponds to the transition from the T-shaped configuration to the face-to-face configuration, which is stable. For $n_b = 3\ \mu m^{-3}$, the energy barrier for this transition is much larger so that it never occurs within the time of simulations. Therefore, the T-shaped doublet is stable at a high enough concentration of rods.

Changes in membrane energy

As mentioned previously, changes in the bending energy due to membrane deformation can be calculated from the 3D reconstruction of the confocal images. Fig. 2 *B* illustrates the distribution of local mean curvature of a single RBC with a biconcave shape, a cell from a parachute doublet, and a cell from a Yin-yang doublet. Single cells retained their original shape for all concentrations of *fd*, as the depletion forces correspond to an isotropic hydrostatic pressure, which does not destabilize the normal shape of RBCs. For the Yin-yang and parachute configurations, the local mean curvature along the rim of a cell increases significantly compared with an undeformed RBC. As a result, the corresponding bending energy must increase for doublet configurations with significant RBC deformation.

Fig. 4 *B* displays the difference in bending energy between an isolated RBC in equilibrium and an RBC from a Yin-yang or parachute doublet as a function of the concentration of *fd* virus or osmotic pressure. As the concentration of *fd* increases, the bending energy of cells for both

Yin-yang and parachute doublets increases. Note that the increase in the bending energy for parachute doublets is less than that for the Yin-yang configuration, indicating less deformation for the case of parachutes. For *fd* concentrations up to 4 mg/ml, RBCs in a Yin-yang doublet experience a moderate deformation and generally preserve their biconcave shape (see Fig. 3 *A*). A further increase in the *fd* concentration finally leads to the limiting case of a nearly spherical doublet. In this spherical Yin-yang configuration for $c_{fd} > 8$ mg/ml, no further excluded volume can be gained. Furthermore, no further bending deformation takes place, and therefore the change in the bending energy levels off. Note that at large c_{fd}, shear deformation and area dilation must still occur, but these contributions to the total energy cannot be accessed by traditional experiments.

To assess other contributions to the total membrane energy, we turn back to simulations. Here, simulations with an attractive potential are used because the strength of depletion interactions in simulations with explicit rods is limited due to the upper limit on the concentration of rods. The rod diameter in simulations is much larger than the *fd* diameter, and therefore the simulated rod suspension undergoes an isotropic-nematic phase transition at elevated concentrations. The red diamonds in Fig. 4 *C* (*full and open*) show the dependence of the two contributions to the membrane energy on the osmotic pressure. The area dilation energy is not shown here as its contribution is negligible compared to the bending and shear deformation energies. At low osmotic pressure, an increase in bending energy with increasing Π is consistent with the increase observed in experiments (see Fig. 4 *B*). For $\Pi \gtrsim 1$ Pa $\left(c_{fd} \gtrsim 8 \text{ mg/ml}\right)$, a substantial increase in the shear deformation energy is observed. Thus, it is plausible to assume that the shear deformation supplies a dominant elastic contribution.

DISCUSSION

Equations 5 and 6 indicate that the osmotic pressure exerted by the rod-like viruses drives the RBC doublet into configurations with a reduced excluded volume, resulting in a cascade of transitions between different cell morphologies (see Fig. 3). These transitions can be understood using the schematic in Fig. 6, which sketches the change in free energy $\Delta E_{\text{tot}} = \Delta E_{\text{dep}} + \Delta E_{\text{def}}$ for different doublet configurations upon increasing the *fd* concentration. In region I, the free energy of undeformed RBCs is minimized (green solid curve). In region II, the shifted gap configuration still has the lowest energy, but the contribution of parachutes to the free energy is increasing so that these different contributions eventually approach each other. In region III, the parachute configuration dominates, but the contribution of Yin-yang configurations takes over with increasing osmotic pressure. Finally, in region IV, the Yin-yang configuration becomes dominant and has the lowest energy (*dashed-dotted blue curve*). This scheme suggests discrete transitions, but, as indicated in Fig. 3, there are extended coexistence regions as the volume of RBCs, and their elastic properties show significant variations as a function of cell age (64). Furthermore, the free energy can vary significantly for different doublets observed under the same depletion conditions due to the variability in RBC properties, such as their age, surface area/volume ratio, viscosity, shear modulus, and bending rigidity.

In region I, RBC doublets in either a T-shaped or face-to-face configuration with a fluctuating gap are observed. Both of these configurations have not been observed previously,

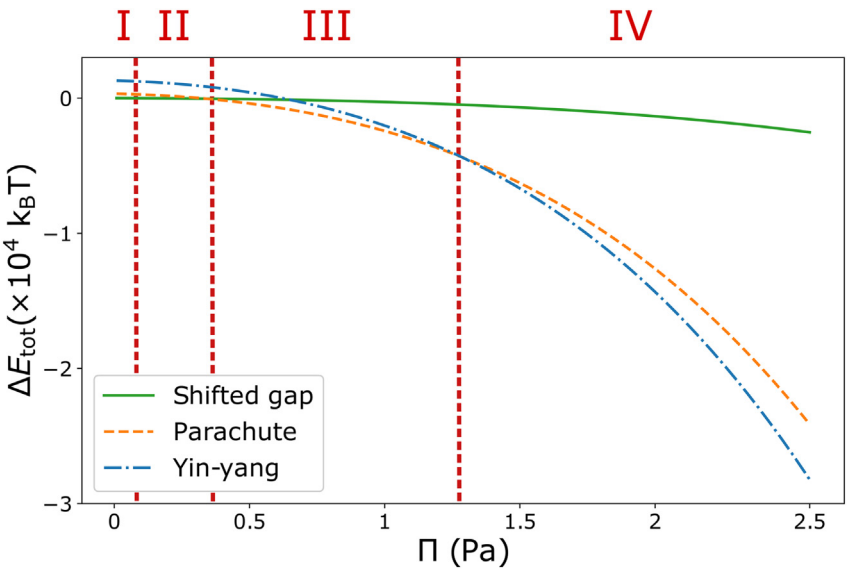

FIGURE 6 Sketch of the free energy gain from doublet formation for three different configurations: shifted gap (*solid green*), parachute (*dashed orange*), and Yin-yang (*dashed-dotted blue*).

which is likely due to the fact that previous studies have employed relatively small depletants, limiting the depletion interaction range. In the current study, rod-like depletants induce an effective and long-range depletion interaction, compared with most previous investigations, due to their high aspect ratio. Indeed, our simulations with explicitly modeled rods as depletants reproduce well the experimental observations. Even though there is nearly no RBC deformation in region I (see Fig. 4 *B*), there is a substantial change in ΔE_{dep} with increasing Π, which can be attributed to the optimization of the doublet configuration through the gain in $V_{\mathrm{ov}}^{\mathrm{conf}}(\boldsymbol{r},\theta)$. An increase in c_{fd} within region I results in a transition from RBC doublet with a fluctuating gap (i.e., with fluctuations in $\boldsymbol{r}$ and θ) at low Π to a face-to-face configuration with a stable (nearly fixed) gap between the cells. For the stable gap, fluctuations in $\boldsymbol{r}$ and θ are substantially reduced, and a full circle-like contact between the RBCs is formed. Despite the fact that the free-volume gain for the rods is larger for the parachute or Yin-yang configurations than for those with a gap, membrane deformation energy is too high to be compensated by the depletion attraction at low rod concentrations.

In region II, a transition from RBC doublets with face-to-face configurations with a gap to RBC doublets with a full surface contact is observed. Here, the gain in the overlap volume primarily originates from closing the gap between two cells in the face-to-face configuration. The gap disappears through the buckling of one of the two dimples. The bottom buckled cell has a slightly higher bending compared with the top cell (see the *open and solid areas* in region II of Fig. 4 *B*). The excluded volume contribution $V_{\mathrm{ex}}(\boldsymbol{r}^{\mathrm{min}},\theta^{\mathrm{min}},\Delta E_{\mathrm{elas}})$ to ΔE_{tot} is large enough to overcome an increase in the deformation energy for the parachute configuration. This energy cost is mainly due to an increase in bending energy upon buckling. With an increase of Π, the fraction of parachute doublets with a full surface contact becomes larger than the fraction of face-to-face configurations with a gap, where the latter practically disappears at $c_{fd} \approx$ 2 mg/ml, and all doublets display a full surface contact (see Fig. 3 *B*). Furthermore, capsule buckling due to an osmotic pressure difference between the interior and exterior of the shell has been reported previously, resulting in a capsule shape with stable dimples (65,66).

In region III, the doublets have full surface contact, and a transition from the parachute to a Yin-yang configuration takes place. For *fd* concentrations slightly above 2 mg/ml, there is no substantial difference in the bending energy penalty between the parachute to Yin-yang configurations (see Fig. 4 *B*). However, with increasing $c_{fd} > 4$ mg/ml, both configurations undergo a sigmoidal transition, where RBCs experience substantial deformation resulting in a reduction of excluded volume (see Fig. 4 *A*). Fig. 4 *C*, where ΔE_{bend} and $|\Delta E_{\mathrm{dep}}|$ are shown by blue bullets (*full and open*, respectively) and directly compared, demonstrates that the change in bending energy is compensated by the change in the depletion energy of parachute and Yin-yang configurations for pressures up to $\Pi \approx 1$ Pa. The simulations indeed confirm that the bending energy is the dominant element in deformation energy for a pairwise adhesion equivalent to a pressure up to $\Pi \approx 1$ Pa. The average change in the bending energy of the cells reaches a plateau at the upper boundary of region III ($c_{fd} \approx 8$ mg/ml) with values of $\Delta E_{\mathrm{bend}} \approx 1 \times 10^3 k_{\mathrm{B}}\mathrm{T}$ in experiments and $\Delta E_{\mathrm{bend}} \approx 1.2 \times 10^3 k_{\mathrm{B}}\mathrm{T}$ in simulations. Note that previous experimental (23) and computational (15,21) investigations have reported only RBC doublets having a full surface contact, which corresponds to the region III of our classification.

Finally, in region IV, $c_{fd} > 8$ mg/ml, the parachute configuration is fully replaced by the Yin-yang configuration, which nearly reaches the most compact configuration of a sphere at $c_{fd} = 12$ mg/ml. While ΔE_{bend} seems to reach a plateau in region IV, $\Delta E_{\mathrm{dep}}^{\mathrm{def}}$ still drops significantly. In this region, the gain in the total depletion free energy is mainly balanced by the elastic shear energy with a smaller contribution of the area dilation energy (data not shown) (see Fig. 4 *C*). The sum of the contributions can be read from Fig. 4 *C*, taking the difference between $|\Delta E_{\mathrm{dep}}|$ and ΔE_{bend}, yielding $\Delta E_{\mathrm{shear}} + \Delta E_{\mathrm{area}} \approx 1.4 \times 10^4 k_{\mathrm{B}}\mathrm{T}$ at $\Pi = 2.2$ Pa. Our simulations also suggest that the energy penalty due to shear deformation can be as large as $10^4 k_{\mathrm{B}}\mathrm{T}$, as E_{shear} displays a steep increase at large attractive strengths between the two RBCs. Using the experimentally determined elastic shear modulus of RBCs in the range $(2-10)\mu\,\mathrm{Nm}^{-1}$ (67–69) and estimation of shear-dominated energy from (28), an estimation of the shear deformation energy of a shell with properties similar to those of RBCs and a radius of 4 μm can be obtained in the range of $\left(0.8 - 4 \times 10^4\right) k_{\mathrm{B}}\mathrm{T}$, in good agreement with our result. There might be additional energetic contributions, such as a deformation of the brush-like glycocalyx in response to applied osmotic pressures. These effects should be, however, less prominent when applying long-ranged depletion interactions mediated by rods compared with smaller depletants such as dextran polymers (7).

In our study, the interaction between two cells induced by rod-like particles is a long-range depletion potential such that no explicit adhesive interactions are present. This depletion interaction leads to a plethora of RBC doublet configurations, most of which can be qualitatively reproduced by simulations with an adhesion potential. When dextran molecules are used as depletants, the interaction between two RBC is more complex, as both bridging and depletion effects are present (23,70). Existing studies on RBC aggregation using fibrinogen show a linear dependence of the attraction energy on fibrinogen concentration, which is similar to *fd* but different from dextran (23,70). Nevertheless, other studies reported binding of fibrinogen to RBCs,

which was not observed for *fd* (25). Therefore, we think that both dextran and fibrinogen likely produce both depletion and adhesion effects, which are difficult to disentangle. Even though the results in Fig. 5 indicate similarities between depletion and attractive-potential interactions, it is not clear whether those two types of interactions are equivalent or not. The amount of data we have is too little to make a definite claim about similarities and differences.

The above-described wealth of configurational transitions is due to the morphology of the RBC with its discoidal shape and high deformability and the use of long rods as depletants. Our findings of the configurational transitions indicate that besides shape (71), deformability is a crucial factor in the self-assembly of soft particles. The wealth of transitions also exemplifies why rods, which can induce forces in the range of 0.6–127 pN, are such effective depletants. First, stable complexes can be induced at very low volume fractions; second, complexes can have a relatively open structure, while being stable (the face-to-face configuration); third, deformations can be induced that are otherwise not feasible. Long-range depletion attraction is especially useful to induce deformation in soft objects. It yields a quantifiable approach that can be applied to other soft objects such as microgels in (72,73). Knowing the depletion force and using the 3D image analysis, we can determine the bending modulus as well as compressibility and elastic behavior of the soft objects. On the other hand, our image analysis can also be directly used to study cell-cell interactions and deformations under pathological conditions such as those caused by sickle cell anemia or malaria, in the case of RBCs.

It is also important to discuss limitations of the proposed approach. The main limitation is that the osmotic pressure induced by depletion is hydrostatic, so dynamic interactions would be difficult to quantify. Therefore, microscopy observations and their quantification should be performed after the system has reached steady state. Furthermore, the quantification of depletion interactions is likely difficult under nonstatic flow conditions, where the overlap volume is time dependent. This method can also be applied to the interaction of cells with solid or deformable substrates. Furthermore, depletion interactions can be used to form aggregates from many (more than two) deformable cells. The quantification of depletion forces and cell deformation within aggregates is expected to be more difficult than for the case of two cells. However, it would be interesting to examine these broader capabilities of the proposed depletion approach in future research.

CONCLUSIONS

Deformation of two RBCs through depletion interactions mediated by nonadsorbing rod-like particles has been investigated using rod-like *fd* virus in experiments and particle-based simulations. A sequence of configurational transitions of RBC doublets with increasing depletant concentration, hence the osmotic pressure, is identified, including configurations that can only be induced by using long-ranged attraction. In the quantitative analysis, a change in the bending energy of single cells in a doublet compared with isolated RBCs has been calculated, as well as a change in the free energy, which characterizes the depletion interaction. At low interaction strengths, the increase in bending energy is balanced by the decrease in depletion energy, as RBCs in a doublet deform to minimize the excluded volume of depletion zones surrounding them. Changes in the shear elasticity become dominant over the bending energy at large interaction strengths, as confirmed by the simulation. As such, we introduced a comprehensive and high-throughput method to study the mechanical features of cells, cell-cell interactions, and pathological deformations using long-ranged depletion interaction and image analysis.

SUPPORTING MATERIAL

Supporting material can be found online at https://doi.org/10.1016/j.bpj.2023.03.030.

AUTHOR CONTRIBUTIONS

M.B. and M.P.L. designed the research. M.B. and M.P.L. performed experiments. D.A.F. performed simulations. A.G. contributed to discussions. J.O. and R.T. contributed to theoretical analysis. M.B., D.A.F., and M.P.L. analyzed data. M.B., D.F., and M.P.L. wrote the article.

ACKNOWLEDGMENTS

M.B. acknowledges support by the International Helmholtz Research School of Biophysics and Soft Matter (IHRS BioSoft). D.A.F. gratefully acknowledges the computing time granted through JARA on the supercomputer JURECA at Forschungszentrum Jülich. J.O. and R.T. acknowledge financial support from the Dutch Ministry of Economic Affairs of the Netherlands via the Top Consortium for Knowledge and Innovation (TKI) roadmap Chemistry of Advanced Materials (grant no. CHEMIE.PGT.2018.006). We thank Thomas Fischer for stimulating discussions.

DECLARATION OF INTERESTS

The authors declare no competing interests.

SUPPORTING CITATIONS

Reference (74) appears in the supporting material.

REFERENCES

1. Zimmerman, S. B., and A. P. Minton. 1993. Macromolecular crowding: biochemical, biophysical, and physiological consequences. *Annu. Rev. Biophys. Biomol. Struct.* 22:27–65.
2. Ellis, R. J. 2001. Macromolecular crowding: obvious but underappreciated. *Trends Biochem. Sci.* 26:597–604.
3. Valkenburg, J. A., and C. L. Woldringh. 1984. Phase separation between nucleoid and cytoplasm in Escherichia coli as defined by immersive refractometry. *J. Bacteriol.* 160:1151–1157.

4. Walter, H., and D. E. Brooks. 1995. Phase separation in cytoplasm, due to macromolecular crowding, is the basis for microcompartmentation. *FEBS Lett.* 361:135–139.
5. Baumler, H., and E. Donath. 1987. Does dextran indeed significantly increase the surface-potential of human red-blood-cells. *Stud. Biophys.* 120:113–122.
6. Bäumler, H., E. Donath, …, H. Kiesewetter. 1996. Electrophoresis of human red blood cells and platelets. Evidence for depletion of dextran. *Biorheology.* 33:333–351.
7. Neu, B., and H. J. Meiselman. 2002. Depletion-mediated red blood cell aggregation in polymer solutions. *Biophys. J.* 83:2482–2490.
8. Baskurt, O. K., and H. J. Meiselman. 2013. Erythrocyte aggregation: basic aspects and clinical importance. *Clin. Hemorheol. Microcirc.* 53:23–37.
9. Tripette, J., T. Alexy, …, P. Connes. 2009. Red blood cell aggregation, aggregate strength and oxygen transport potential of blood are abnormal in both homozygous sickle cell anemia and sickle-hemoglobin C disease. *Haematologica.* 94:1060–1065.
10. Maciaszek, J. L., and G. Lykotrafitis. 2011. Sickle cell trait human erythrocytes are significantly stiffer than normal. *J. Biomech.* 44:657–661.
11. Reichel, F., M. Kräter, …, J. Guck. 2022. Changes in blood cell deformability in Chorea-Acanthocytosis and effects of treatment with dasatinib or lithium. *Front. Physiol.* 13
12. Asakura, S., and F. Oosawa. 1954. On interaction between two bodies immersed in a solution of macromolecules. *J. Chem. Phys.* 22:1255–1256.
13. Forth, S., C. Deufel, …, M. D. Wang. 2008. Abrupt buckling transition observed during the plectoneme formation of individual DNA molecules. *Phys. Rev. Lett.* 100:148301.
14. Leijnse, N., L. B. Oddershede, and P. M. Bendix. 2015. Helical buckling of actin inside filopodia generates traction. *Proc. Natl. Acad. Sci. USA.* 112:136–141.
15. Hoore, M., F. Yaya, …, D. A. Fedosov. 2018. Effect of spectrin network elasticity on the shapes of erythrocyte doublets. *Soft Matter.* 14:6278–6289.
16. Bergman, M. J., N. Gnan, …, P. Schurtenberger. 2018. A new look at effective interactions between microgel particles. *Nat. Commun.* 9:5039.
17. Rovigatti, L., N. Gnan, …, E. Zaccarelli. 2015. How soft repulsion enhances the depletion mechanism. *Soft Matter.* 11:692–700.
18. Lekkerkerker, H. N., and R. Tuinier. 2011. Depletion interaction. *In* Colloids and the Depletion Interaction Springer, pp. 57–108.
19. Sacanna, S., W. T. M. Irvine, …, D. J. Pine. 2010. Lock and key colloids. *Nature.* 464:575–578.
20. Nehring, A., T. N. Shendruk, and H. W. de Haan. 2018. Morphology of depletant-induced erythrocyte aggregates. *Soft Matter.* 14:8160–8171.
21. Ziherl, P., and S. Svetina. 2007. Flat and sigmoidally curved contact zones in vesicle–vesicle adhesion. *Proc. Natl. Acad. Sci. USA.* 104:761–765.
22. Murakami, K., R. Ebihara, …, M. Imai. 2020. Morphologies of vesicle doublets: competition among bending elasticity, surface tension, and adhesion. *Biophys. J.* 119:1735–1748.
23. Flormann, D., O. Aouane, …, C. Wagner. 2017. The buckling instability of aggregating red blood cells. *Sci. Rep.* 7:7928–8010.
24. Chien, S., S. Usami, …, M. I. Gregersen. 1966. Effects of hematocrit and plasma proteins on human blood rheology at low shear rates. *J. Appl. Physiol.* 21:81–87.
25. Korculanin, O., T. Kochetkova, and M. P. Lettinga. 2021. Competition between red blood cell aggregation and breakup: depletion force due to filamentous viruses vs. Shear flow. *Front. Phys.* 9. https://www.frontiersin.org/article/10.3389/fphy.2021.721368.
26. Guu, D., J. K. G. Dhont, …, M. P. Lettinga. 2012. Depletion induced clustering in mixtures of colloidal spheres and fd-virus. *J. Phys. Condens. Matter.* 24:464101.
27. Opdam, J., D. Guu, M. P. M. Schelling, D. G. A. L. Aarts, R. Tuinier, and M. P. Lettinga. 2021. Phase stability of colloidal mixtures of spheres and rods. *J. Chem. Phys.* 154:204906.
28. Nayani, K., A. A. Evans, …, N. L. Abbott. 2020. Dynamic and reversible shape response of red blood cells in synthetic liquid crystals. *Proc. Natl. Acad. Sci. USA.* 117:26083–26090.
29. Bader, D. L., and M. M. Knight. 2008. Biomechanical analysis of structural deformation in living cells. *Med. Biol. Eng. Comput.* 46:951–963.
30. Foster, K. M., D. V. Papavassiliou, and E. A. O'Rear. 2021. Elongational stresses and cells. *Cells.* 10:2352.
31. Nelson, C. M., R. P. Jean, …, C. S. Chen. 2005. Emergent patterns of growth controlled by multicellular form and mechanics. *Proc. Natl. Acad. Sci. USA.* 102:11594–11599.
32. Goldblatt, Z. E., H. A. Cirka, and K. L. Billiar. 2021. Mechanical regulation of apoptosis in the cardiovascular system. *Ann. Biomed. Eng.* 49:75–97.
33. Eisenhoffer, G. T., P. D. Loftus, …, J. Rosenblatt. 2012. Crowding induces live cell extrusion to maintain homeostatic cell numbers in epithelia. *Nature.* 484:546–549.
34. Marinari, E., A. Mehonic, …, B. Baum. 2012. Live-cell delamination counterbalances epithelial growth to limit tissue overcrowding. *Nature.* 484:542–545.
35. Davies, P. F. 1995. Flow-mediated endothelial mechanotransduction. *Physiol. Rev.* 75:519–560.
36. Dong, C., J. Cao, …, H. H. Lipowsky. 1999. Mechanics of leukocyte deformation and adhesion to endothelium in shear flow. *Ann. Biomed. Eng.* 27:298–312.
37. Chien, S., S. Usami, …, M. I. Gregersen. 1970. Shear-dependent deformation of erythrocytes in rheology of human blood. *Am. J. Physiol.* 219:136–142.
38. Musielak, M. 2009. Red blood cell-deformability measurement: review of techniques. *Clin. Hemorheol. Microcirc.* 42:47–64.
39. Arbore, C., L. Perego, …, M. Capitanio. 2019. Probing force in living cells with optical tweezers: from single-molecule mechanics to cell mechanotransduction. *Biophys. Rev.* 11:765–782.
40. Hochmuth, R. M. 2000. Micropipette aspiration of living cells. *J. Biomech.* 33:15–22.
41. Evans, E. A. 1973. New membrane concept applied to the analysis of fluid shear-and micropipette-deformed red blood cells. *Biophys. J.* 13:941–954.
42. Evans, E. A., R. Waugh, and L. Melnik. 1976. Elastic area compressibility modulus of red cell membrane. *Biophys. J.* 16:585–595.
43. Evans, E. A. 1983. Bending elastic modulus of red blood cell membrane derived from buckling instability in micropipet aspiration tests. *Biophys. J.* 43:27–30.
44. Dao, M., C. T. Lim, and S. Suresh. 2003. Mechanics of the human red blood cell deformed by optical tweezers. *J. Mech. Phys. Solid.* 51:2259–2280.
45. Brandão, M. M., A. Fontes, …, S. T. O. Saad. 2003. Optical tweezers for measuring red blood cell elasticity: application to the study of drug response in sickle cell disease. *Eur. J. Haematol.* 70:207–211.
46. Radmacher, M. 1997. Measuring the elastic properties of biological samples with the AFM. *IEEE Eng. Med. Biol. Mag.* 16:47–57.
47. Bremmell, K. E., A. Evans, and C. A. Prestidge. 2006. Deformation and nano-rheology of red blood cells: an AFM investigation. *Colloids Surf. B Biointerfaces.* 50:43–48.
48. Baier, D., T. Müller, …, U. Windberger. 2021. Red blood cell stiffness and adhesion are species-specific properties strongly affected by temperature and medium changes in single cell force spectroscopy. *Molecules.* 26:2771.
49. Fedosov, D. A., B. Caswell, and G. E. Karniadakis. 2010. A multiscale red blood cell model with accurate mechanics, rheology, and dynamics. *Biophys. J.* 98:2215–2225.

50. Fedosov, D. A., B. Caswell, and G. E. Karniadakis. 2010. Systematic coarse-graining of spectrin-level red blood cell models. *Comput. Methods Appl. Mech. Eng.* 199:1937–1948.

51. Gompper, G., and D. M. Kroll. 1996. Random surface discretizations and the renormalization of the bending rigidity. *J. Phys. I France.* 6:1305–1320.

52. Lekkerkerker, H. N. W., and A. Stroobants. 1994. Phase behaviour of rod-like colloid+ flexible polymer mixtures. *Il Nuovo Cimento D.* 16:949–962.

53. Cotter, M. A., and D. E. Martire. 1970. Statistical mechanics of rodlike particles. II. A Scaled Particle investigation of the aligned →isotropic transition in a fluid of rigid spherocylinders. *J. Chem. Phys.* 52:1909–1919.

54. Grelet, E., and S. Fraden. 2003. What is the origin of chirality in the cholesteric phase of virus suspensions? *Phys. Rev. Lett.* 90:198302.

55. Asakura, S., and F. Oosawa. 1958. Interaction between particles suspended in solutions of macromolecules. *J. Polym. Sci.* 33:183–192.

56. Lin, K.-h., J. C. Crocker, …, A. G. Yodh. 2001. Colloidal interactions in suspensions of rods. *Phys. Rev. Lett.* 87:088301.

57. Holmqvist, P., D. Kleshchanok, and P. R. Lang. 2008. Interaction potential and near wall dynamics of spherical colloids in suspensions of rod-like fd-virus. *Eur. Phys. J. E Soft Matter.* 26:177–182.

58. Sambrook, J., D. W. Russell, and J. Sambrook. 2006. The Condensed Protocols: From Molecular Cloning: a Laboratory Manual. Sirsi) I9780879697723. Cold Spring Harbor Laboratory Press Cold Spring Harbor.

59. Berg, S., D. Kutra, …, A. Kreshuk. 2019. ilastik: interactive machine learning for (bio)image analysis. *Nat. Methods.* 16:1226–1232. https://doi.org/10.1038/s41592-019-0582-9.

60. Cignoni, P., M. Callieri, …, G. Ranzuglia. 2008. MeshLab: an open-source mesh processing tool. *In* Eurographics Italian Chapter Conference. V. Scarano, R. D. Chiara, and U. Erra, eds The Eurographics Association.

61. Allen, M. P., and D. J. Tildesley. 1991. Computer Simulation of Liquids. Clarendon Press.

62. Jülich Supercomputing Centre. 2021. JURECA: data centric and booster modules implementing the modular supercomputing architecture at Jülich supercomputing centre. *J. Large-Scale Res. Facil.* 7:A182.

63. Skalak, R., P. R. Zarda, …, S. Chien. 1981. Mechanics of rouleau formation. *Biophys. J.* 35:771–781.

64. Kim, J., H. Lee, and S. Shin. 2015. Advances in the measurement of red blood cell deformability: a brief review. *J. Cell. Biotechnol.* 1:63–79.

65. Datta, S. S., S.-H. Kim, …, D. A. Weitz. 2012. Delayed buckling and guided folding of inhomogeneous capsules. *Phys. Rev. Lett.* 109:134302.

66. Knoche, S., and J. Kierfeld. 2014. Osmotic buckling of spherical capsules. *Soft Matter.* 10:8358–8369.

67. Hénon, S., G. Lenormand, …, F. Gallet. 1999. A new determination of the shear modulus of the human erythrocyte membrane using optical tweezers. *Biophys. J.* 76:1145–1151.

68. Engelhardt, H., and E. Sackmann. 1988. On the measurement of shear elastic moduli and viscosities of erythrocyte plasma membranes by transient deformation in high frequency electric fields. *Biophys. J.* 54:495–508.

69. Waugh, R., and E. A. Evans. 1979. Thermoelasticity of red blood cell membrane. *Biophys. J.* 26:115–131.

70. Lee, K., M. Kinnunen, …, A. A. Fedyanin. 2016. Optical tweezers study of red blood cell aggregation and disaggregation in plasma and protein solutions. *J. Biomed. Opt.* 21:035001.

71. van Anders, G., D. Klotsa, …, S. C. Glotzer. 2014. Understanding shape entropy through local dense packing. *Proc. Natl. Acad. Sci. USA.* 111:E4812–E4821.

72. Scotti, A., U. Gasser, …, J. E. Houston. 2022. Experimental determination of the bulk moduli of hollow nanogels. *Soft Matter.* 18:5750–5758. https://doi.org/10.1039/D2SM00680D.

73. Sierra-Martin, B., J. A. Frederick, …, A. Fernandez-Nieves. 2011. Determination of the bulk modulus of microgel particles. *Colloid Polym. Sci.* 289:721–728.

74. Oversteegen, S. M., and H. N. W. Lekkerkerker. 2004. Phase diagram of mixtures of hard colloidal spheres and discs: a free-volume scaled-particle approach. *J. Chem. Phys.* 120:2470–2474.